Article

On-Site Stability Assessment of Rubble Mound Breakwaters Using Unmanned Aerial Vehicle-Based Photogrammetry and Random Sample Consensus

Marcos Arza-García [1,2,*], José Alberto Gonçalves [2], Vladimiro Ferreira Pinto [2] and Guillermo Bastos [1]

1   CIGEO—Civil & Geomatics Research Group, Higher Polytechnic School of Engineering (EPSE), University of Santiago de Compostela, 27002 Lugo, Spain; inardesign.gbastos@uvigo.es
2   CICGE—Geospatial Sciences Research Centre, Faculty of Sciences (FCUP), University of Porto, 4169-007 Porto, Portugal; jagoncal@fc.up.pt (J.A.G.); geral@topogonal.com (V.F.P.)
*   Correspondence: m.arza@usc.es

Abstract: Traditional methods for assessing the stability of rubble mound breakwaters (RMBs) often rely on 2.5D data, which may fall short in capturing intricate changes in the armor units, such as tilting and lateral shifts. Achieving a detailed analysis of RMB geometry typically requires fully 3D methods, but these often hinge on expensive acquisition technologies like terrestrial laser scanning (TLS) or airborne light detection and ranging (LiDAR). This article introduces an innovative approach to evaluate the structural stability of RMBs by integrating UAV-based photogrammetry and the random sample consensus (RANSAC) algorithm. The RANSAC algorithm proves to be an efficient and scalable tool for extracting primitives from point clouds (PCs), effectively addressing challenges presented by outliers and data noise in photogrammetric PCs. Photogrammetric PCs of the RMB, generated using Structure-from-Motion and MultiView Stereo (SfM-MVS) from both pre- and post-storm flights, were subjected to the RANSAC algorithm for plane extraction and segmentation. Subsequently, a spatial proximity criterion was employed to match cuboids between the two time periods. The methodology was validated on the detached breakwater of Cabedelo do Douro in Porto, Portugal, with a specific focus on potential rotations or tilting of Antifer cubes within the protective layer. The results, assessing the effects of the Leslie storm in 2018, demonstrate the potential of our approach in identifying and quantifying structural changes in RMBs.

Keywords: drone; RMB; groins; in-field inspection; photogrammetry; SfM-MVS; random sample consensus

1. Introduction

The protection of coastal zones and harbors from wave damage is crucial to prevent severe economic and ecological consequences. One of the most commonly employed structures for this purpose are the rubble-mound breakwaters (RMBs). These structures are built using various materials and can be adapted to diverse underwater topographies, designed to withstand different wave conditions [1]. However, these protective structures are susceptible to damage and require repairs throughout their lifespan [2]. Therefore, understanding the performance of rubble-mound armor in terms of hydraulic stability is essential for designing new structures and upgrading existing ones, particularly in light of climate change effects such as sea level rise and increased wave storminess [3,4].

Detecting local defects in coastal defense structures, like displacements, breakage, or removals of concrete armor units (CAUs), is crucial to prevent potential threats to the safety of breakwaters. Damages observed in these structures can lead to sliding, settlement, or toppling, causing the displacement, breakage, or removal of CAUs. Additionally, scouring at dike foundations may occur and result in severe damages under extreme wave forces from storms. Identifying local shifts in the elements of these structures would be beneficial for studying their performance and mitigating damages caused by potential defects [5].

Techniques for assessing and measuring lab-scale physical models, with a focus on examining the behavior of RMBs under wave action, have advanced significantly in recent years. Laboratory investigations exploring this subject employ a range of scanning devices, including structured light scanners, infrared scanners, and laser scanners, along with conventional profilers [6]. Some studies have also integrated devices with additional depth measurement capabilities, such as time-of-flight (ToF) and RGB-D cameras (e.g., Kinect) [7–10], providing the advantage of collecting information from the submerged portions of RMB models. Image-based methodologies are also increasingly utilized [11], with a specific subset of studies concentrating on photogrammetric reconstruction [12,13] to achieve a detailed three-dimensional representation of the slopes.

However, unlike laboratory testing of physical models, the field of on-site monitoring of RMBs still has ample room for further advancement in both research and the development of assessment methodologies. Currently, the evaluation of the current maintenance conditions in RMBs and groins typically relies heavily on visual inspections to assess structural damage. Whether conducted during routine monitoring campaigns or post-storm assessments, these inspections provide essential insights for improving breakwater design and maintenance, ensuring their long-term effectiveness. Nevertheless, developing standardized and more efficient methodologies for the in-field evaluation of RMB damage remains a challenging task due to the significant variability in construction from site to site, as well as associated costs and safety considerations.

1.1. SfM-MVS Photogrammetry in RMB Inspection

Terrestrial photogrammetry [14] and terrestrial laser scanning (TLS) [5] have proven to be efficient techniques for examining changes in small dikes or RMBs using point clouds (PCs) derived from different epochs. Nevertheless, the advent of uncrewed aerial vehicles (UAVs) has revolutionized coastal monitoring, offering a cost-effective, flexible, and high-resolution approach to data collection across large areas [15]. While UAVs can be equipped with various sensors, such as UAV-borne LIDAR, affordable and lightweight RGB cameras have become the standard for remote sensing and photogrammetric research. In this context, the photogrammetric applications of these tools in the field are diverse, encompassing tasks such as investigating near-shore hydrodynamics [16], mapping and quantifying volumetric changes on beaches [17], and inspecting offshore civil infrastructures [18]. The integration of UAVs into such tasks not only establishes a robust toolkit for detailed photogrammetric reconstructions and analyses but also introduces real-time monitoring capabilities, particularly crucial after severe events [19]. UAV-based photogrammetry has also proven to be a useful reverse engineering technique, providing data on actual morphologies that can be translated into numerical analyses in different applications (e.g., flooding risk assessment [20], slope stability analysis [21], erosion and accretion studies [22], etc.). However, it is important to acknowledge that the use of UAV-based photogrammetry in water-related studies is not without challenges. Addressing concerns such as limitations in flight time, payload capacity considerations, legal issues, drone security, and varying data acquisition conditions remains critical in some applications [15].

Specific applications of UAV-based surveys in rubble mound groins can be found in previous research, such as in the work of Henriques et al., 2017 [23], which generated photogrammetric orthomosaics and PCs to obtain data about the most exterior protection layer of breakwaters. Gonçalves et al. 2022a and 2022b [24,25] expanded the photogrammetric workflow by incorporating UAV-based real-time kinematic (RTK) data to accurately map the geometry of rubble mound groins. They also conducted an accuracy assessment using independent techniques (i.e., GNSS and TLS). These previous studies demonstrate the potential of UAV-based photogrammetry in monitoring the structural integrity by generating three-dimensional (3D) geometric reconstructions of RMBs, achieving accuracies in some cases better than 3 cm of error in checkpoints. In this regard, UAV-based photogrammetry has proven to be a highly suitable technique to obtain detailed and precise 3D reconstructions, particularly advantageous when dealing with large, complex,

and potentially hazardous structures like these. However, to the best of our knowledge, there is still insufficient research on multi-temporal monitoring of RMBs using UAV-based photogrammetry. More specifically, there is a clear shortage of studies exploring possible methods of automatic change detection.

1.2. Change Detection Analysis in RMBs

Change detection poses a critical challenge in various remote sensing applications. Historically, studies within this domain have relied on 2D information from remote sensing images to address large-scale issues, such as forest monitoring or urban sprawl. Previous research has dedicated significant efforts to developing new methods for detecting changes from images, starting with traditional/classical pixel-based methods that primarily focus on spectral values [26]. More recently, methods in geographic object-based image analysis (GEOBIA) have emerged [27,28], introducing innovative segmentation and classification techniques that consider spatial context along with spectral, topographical, textural, and morphological properties. The emergence of new detectors and feature descriptors has gone beyond the limitations of traditional top-view 2D pixel/object-based analyses [29,30], playing a pivotal role in applications like security and surveillance, infrastructure monitoring, or precision agriculture [31]. However, as image resolution advances to finer levels, several challenges arise when employing 2D image-based methods. Issues like spectral variability and perspective distortion become prominent. In response to these challenges, the incorporation of 3D data in finer-scale studies introduces a different modality for analysis, enabling highly detailed geometric analysis [32].

Among the common techniques used to identify changes from 3D datasets acquired at different time intervals, cross-sectional assessment or the simple comparison of digital surface models (DSM), also known as the DEM of Difference (DoD) method [33], are frequently employed. However, these techniques still predominantly rely on 2.5D information as they primarily operate within a 2D spatial framework, despite considering the elevation or height of objects [34]. In contrast, the damage progression along a sloping coastal structure like a rubble-mound breakwater (RMB) is fundamentally a 3D process. It is crucial to recognize that objects may undergo vertical shifts, rotations, or tilting, emphasizing the need for approaches that can capture and analyze changes in the full 3D spatial context.

On the other hand, methods lacking full 3D spatial information often struggle to differentiate individual armor units, reducing possibilities for subsequent analysis. While the simpler DoD approach can be useful for estimating erosion volume in the breakwater, a more detailed assessment can be carried out at the individual block level. This approach yields more precise statistics and provides a more reliable count of the displaced armor units [6].

Earlier investigations aimed to refine methods for estimating poses of individual blocks, though there is a relative absence of applications on dense PCs obtained directly from on-site photogrammetric surveys. In a study conducted by Puente et al. in 2014 [5], changes in RMBs were examined using TLS PCs from different time periods. To estimate the rigid body transformation parameters, they employed K-means clustering to identify planar segments representing the faces of the cuboids. Bueno Esposito et al., in 2015 [35], presented an approach for reconstructing wave-dissipating blocks from incomplete PCs of RMBs captured by airborne LiDAR. Their method used segmentation based on normal vectors and prior knowledge about the properties of the cuboids to refine the segmentation and define the boundaries of individual armor units. Xu et al., in 2022 [36], presented a deep-learning-based approach for block pose identification that could even identify CAUs with complex shapes, such as tetrapods or clinger blocks. However, this method entails the need for extensive training datasets to feed the convolutional neural network and substantial computational resources, which may present implementation difficulties and necessitate site-specific fine-tuning.

Although not specifically applied to RMBs, Shen et al., in 2018 [37], presented a methodology to extract individual brick poses from a laser scan PC of a cluttered pile of

cuboid bricks. Their proposed workflow includes connected component analysis, principal component analysis, and a voting scheme to reconstruct bricks individually. Shen, Wang, and Puente in 2020 [38] proposed a method for detecting changes in masonry walls using TLS PCs with a regular distribution of bricks, a case study analogous to cube-armored breakwaters with a regular placement pattern. They utilized the TLS intensity attribute to differentiate between materials of mortar and bricks, followed by a 3D connected components algorithm to extract and label individual bricks.

1.3. The RANSAC Approach

While there are multiple valid strategies in the statistics field for determining block pose through surface extraction, several of the reviewed solutions may suffer from practical limitations, such as computational intensity, implementation complexity, and sensitivity to data noise [39]. For instance, the M-estimator, L-estimator, R-estimator [40], and Least Median of Squares (LMedS) [41] methods approached regression with outliers as a minimization problem, akin to the least square method that minimizes the sum of squared error values. However, they employed nonlinear and intricate loss functions instead of the square of the error. LMedS aimed to minimize the median of the error values, requiring a numerical optimization algorithm to solve such nonlinear minimization problems. The 3D Hough [42] method transforms spatial data (e.g., 3D points corresponding to a plane) from the 3D data space into a parameter space (e.g., normal vector components and distance from the origin). The most prevalent point in the parameter space is identified as its estimation, demanding a significant amount of memory to represent the parameter space. As stated before, deep learning methods, such as convolutional neural networks (CNNs) for 3D pose estimation [43], have also gained popularity. However, they may face challenges such as high computational resource requirements, the need for large training datasets, and complexity in adapting to different scenarios.

In contrast to the aforementioned methods, the random sample consensus (RANSAC) algorithm [44] simplifies the process into two steps: generating a hypothesis from random samples and verifying it against the data. This approach eliminates the need for complex optimization algorithms and large memory allocations. In that sense, RANSAC can robustly work in a wide range of applications and with several sources of data (e.g., TLS, photogrammetry), even if these data include more than 50% of outliers [45]. Besides its enhanced computational efficiency, RANSAC presents another important advantage in its scalability concerning the size of the input PC and the number and size of the shapes within the data.

This algorithm has already been validated in other applications, such as the automatic extraction of building elements (e.g., roof planes and walls) [46,47], structural planes of rocky slopes [48], water-level planes [49], etc. In these studies, the application of RANSAC has demonstrated efficient performance, even in photogrammetric PCs, which are typically noisier than those obtained through TLS or LiDAR.

This article introduces a novel methodology for monitoring the structural stability of wave-dissipating cuboids of RMBs using UAV-based photogrammetric surveys and RANSAC-based segmentation. To assess the practicality and performance of this approach, we conduct a case study application on a detached breakwater that has experienced damage due to a severe maritime storm. This case study aims to evaluate the effectiveness of the proposed RANSAC-based approach in comparison to traditional methods such as the Difference of Digital Surface Models (or DoD), particularly in the context of detecting and quantifying changes like tilting in individual armor units. The methodology enables the generation of quantitative insights into the extent of damage and the overall structural integrity of the RMB, facilitating the conduction of a zonal stability analysis for this breakwater.

2. Materials and Methods

2.1. Study Site

Located at the mouth of the Douro River in Porto, Portugal, the Cabedelo do Douro area (41°08′N, 8°40′W) has a detached breakwater designed for shore protection due to the significant wave energy in this coastal zone. The RMB plays a crucial role in shielding the Douro River estuary from the Atlantic waves. Its strategic location reinstates the protective function of the sand spit, ensuring the safety of ships and boats navigating through the area [50].

The RMB was constructed with a curved shape, spanning approximately 450 m in the southeast to northwest direction, and its concavity faces the land (Figure 1). The relatively low crest elevation, standing at +6.0 m above mean sea level (AMSL), minimizes its visual impact on the landscape. The structure comprises a rockfill core, overlaid by secondary layers of granite blocks, featuring filter functions and an outer protective layer. This protective layer consists of high-density concrete grooved cuboids (Antifer type) weighing 8 kN, initially arranged in a regular placement pattern.
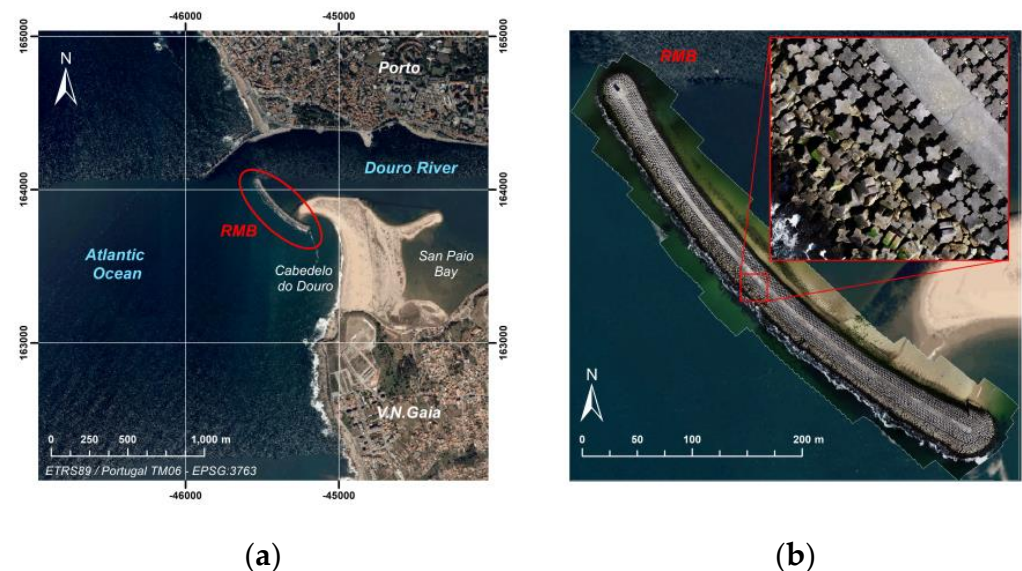

(**a**)   (**b**)

Figure 1. Location of the structure within the mouth of Douro River (**a**), and (**b**) detailed view of the RMB.

2.2. Field Campaigns

Two flight campaigns were conducted on 12 September and 27 November 2018, with the aim of capturing potential displacements of the armor units. While the interval between the dates may appear short for detecting significant displacements, this period allows for the analysis of the impact of Hurricane Leslie (13–14 October 2018) on the structure. The hurricane, also known as Leslie storm in Spain and Portugal once in the extratropical category, was the most powerful cyclone to reach the Iberian Peninsula since 1842 and one of the longest-lasting Atlantic hurricanes over time. In this sense, the test field provides an excellent environment for validating the methods and detecting potential movements in CAUs.

The aerial images were captured using a UAV Phantom 4 Pro v.2 equipped with a built-in camera (Table 1). All flights were planned using Pix4DCapture (Pix4D, Lausanne, Switzerland) v.4.2.0 following a grid pattern along the breakwater and the adjacent coast, capturing overlapping images (Table 2). The flight speed was set to an intermediate value in the Pix4D app, which, after calculations, resulted in approximately 2.3 m/s.

Table 1. Specifications of UAV Phantom 4 Pro quadcopter.

|	
Weight	1388 g
Max Wind Speed Resistance	10 m/s
Max Flight Time	Approx. 30 min
GNSS Positioning	GPS/GLONASS
Hover Accuracy Range	Vertical: 0.5 m (GPS positioning)
	Horizontal: 1.5 m (GPS positioning)
Camera resolution	20 megapixels
Sensor size	1-inch CMOS

Table 2. Flight planning parameters.

Altitude for Mapping Mission	30 m
Frontlap	80%
Sidelap	60%
Ground Sample Distance	<1 cm
Speed of Flight	2.3 m/s
Mission Area	2.33 ha

The required level of detail is commonly associated with the concept of ground sampling distance (GSD), which represents the real-world size of an element represented by a single pixel. The GSD can be calculated based on the focal length (f), shooting distance (d), and pixel size (p), as shown in Equation (1) [51]. According to that equation and the camera specifications, the flight altitude was set at 30 m above the ground level to obtain images with GSD values less than 1 cm.

$$\text{GSD} = \frac{d}{f} \cdot p \tag{1}$$

The field operations involving the marking and measurement of ground control points (GCPs) and checkpoints (CPs) were carried out on the same day, immediately preceding each flight. The points were marked on the ground using paint. For the georeferencing of each point, three readings were recorded, and an average was calculated. This process was conducted in real-time kinematic (RTK) mode using double-frequency GNSS equipment with centimetric precision (Leica GNSS Smart Rover 1200). Differential corrections were obtained from the Portuguese DGT's ReNEP reference stations. Topologically, the scene's geometry is a linear acquisition, and such image distribution tends to produce the bending or "dome" effect in photogrammetry. To mitigate this effect, a total of 48 points, forming 7 groups/rows distributed along the central corridor, were selected and measured as illustrated in Figure 2. Subsequently, 8 of these points were chosen as CPs to validate accuracies.
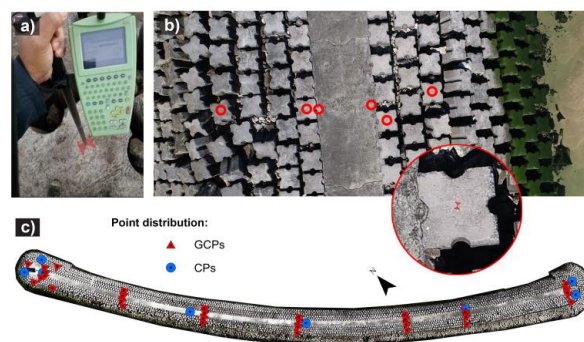
Figure 2. Ground control. (**a**) GNSS receiver and distribution of the GCPs and checkpoints along (**b**) rows and (**c**) the whole RMB.

2.3. Flowchart of the Process

The methodological flow of this study, depicted in Figure 3, is based on the conventional Structure-from-Motion and MultiView Stereo (SfM-MVS) photogrammetric pipeline. Subsequently, RANSAC is employed for plane extraction, as detailed in the following sections.
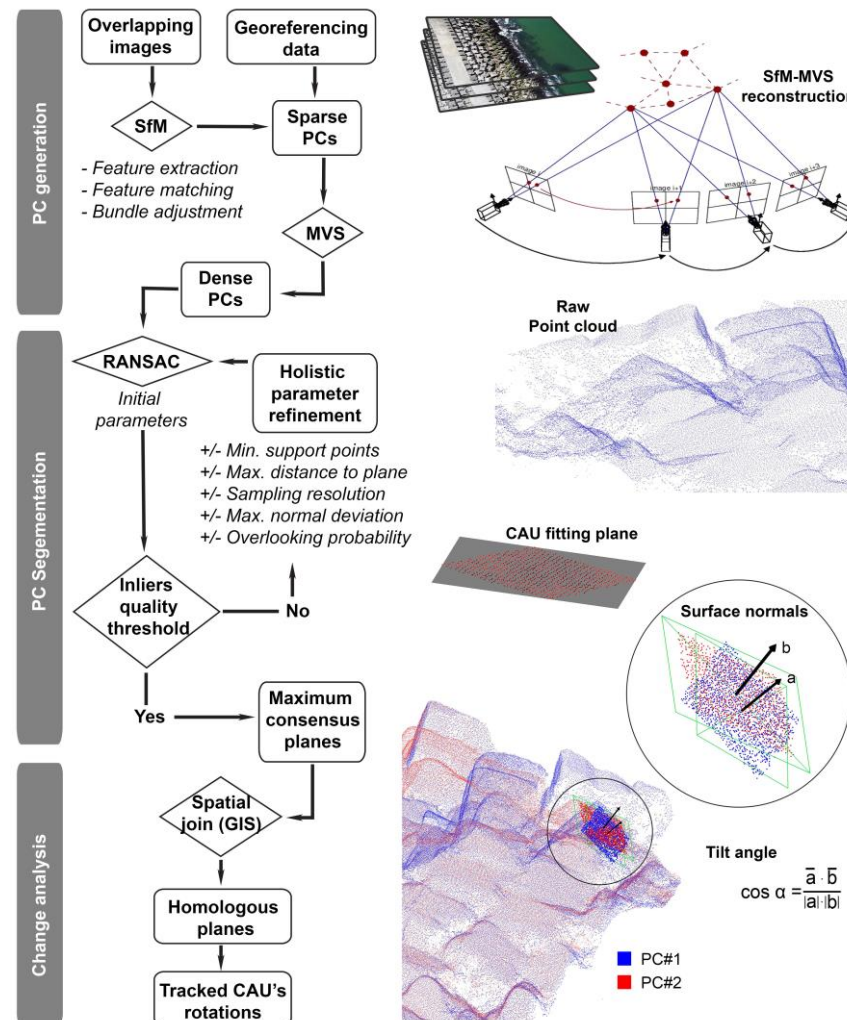

Figure 3. Workflow of the methodology implemented in this study.

2.4. Photogrammetric Reconstruction

SfM-MVS photogrammetry is recognized as a pivotal technique for reconstructing 3D scenes from a set of overlapping 2D images [52,53]. Image processing based on these algorithms involves a series of steps, collectively referred to as the photogrammetric workflow, which facilitates the generation of dense PCs. The core of the photogrammetric workflow lies in the SfM reconstruction (see Figure 3), commencing with (i) key feature extraction, where distinctive (key) points are identified in the input images. These features are extracted by the software, using techniques like Scale-Invariant Feature Transform (SIFT) or Speeded-Up Robust Features (SURF) and serve as the foundation for subsequent stages. Following feature extraction, (ii) a feature matching process is undertaken to establish correspondences between key points across different images. The matched points (namely, tie points) extracted from the images enable the determination of the initial camera positions and matched points in 3D space. These initial estimates are then refined using (iii) bundle adjustment, which iteratively adjusts the camera poses to minimize inconsistencies and enhance the overall accuracy of the reconstruction. By incorporating GCPs into

bundle adjustment, external calibration sources are introduced, aligning the reconstruction with real-world coordinates. This alignment compensates for distortions from factors like lens aberrations and sensor imprecisions, thereby enhancing the overall reliability of the reconstruction.

Another component of the workflow is (iv) Multi-View Stereo (MVS), where the initial sparse PCs undergo further refinement and densification to generate a dense PC. Multi-view stereo algorithms, such as Semi-Global Matching (SGM) or PatchMatch Stereo, leverage the geometry and photometric information across multiple views to produce detailed and high-density PCs representing the scene geometry.

To process the aerial datasets of the RMB, we implemented the photogrammetric pipeline using Metashape software (Agisoft, St. Petersburg, Russia) v2.0.2 within a cloud-based infrastructure configured with 64vCPU, @2.3 GHz, 488 GB RAM, 4x Nvidia Tesla M60/32 GB. This setup ensures the computational power necessary for the efficient processing of the aerial datasets. Table 3 outlines the key photogrammetric processing parameters employed in Metashape.

Table 3. Photogrammetric processing parameters.

Image Alignment Method	Adaptive camera model
Alignment Accuracy	High (original image size)
Key Point Limit	50,000
Tie Point Limit	10,000
Depth Maps Quality	High
Filtering Mode	Aggressive

2.5. RANSAC-Based Segmentation

The RANSAC method is a robust algorithm commonly employed for model fitting and segmentation in PCs, enabling their partitioning into simple shapes such as planes, spheres, cylinders, cones, tori, etc. The algorithm operates by iteratively selecting a random subset of points from the input data and fitting a model to these points. The model is then evaluated by counting the number of inliers, which are points that align with the model within a certain threshold [45].

The objective was to use this algorithm to extract planar patches representing the upper faces of the Antifer cuboids of the RMB. Therefore, parameters corresponding to the mathematical model and termination conditions were defined before the iteration process, depending on the characteristics of the PCs. The regularity of the cuboids played an important role, allowing the fine-tuning of parameters based on the results until a certain level of correctness and completeness was achieved. These parameters include the minimum number of points required to form a plane and other thresholds for inlier selection, such as the maximum distance to the plane, the maximum angular deviation of the plane's normal, etc.

A consensus solution was obtained as the best result after k iterations, approximately determined as a function of the desired probability, according to the following equation [54]:

$$k = \frac{\log(1 - z)}{\log(1 - w^n)} \tag{2}$$

where z represents the minimal probability of success in finding at least one proper set of observations, w denotes the percentage probability of observations allowed to be incorrect, and n is the minimal number of points necessary for computing the model.

Once the best model has been identified (i.e., the one with the largest number of inliers), the corresponding consensus planes were extracted by selecting all the inliers consistent with the models. This process was executed on the two photogrammetric PCs using the RANSAC Shape Detection algorithm implemented in CloudCompare software (GNU GPL), v.2,13, with the same parameters, resulting in two segmented PCs.

2.6. RMB Change Analysis

The RANSAC algorithm functions as a surface extraction process, identifying planar segments representing the upper faces of each CAU one by one. The results are then exported as separate entities, with the detected planes having associated attributes, including coordinates defining their centers {Cx, Cy, Cz} and normal vectors {Nx, Ny, Nz}. However, at this stage, there is no direct plane-to-plane correspondence between the cuboids of PC#1 and their counterparts in PC#2. To establish this correspondence, we employed the criterion of proximity, utilizing a GIS tool called "spatial join". This tool assigns each entity with all attributes of the corresponding one in the layer being joined that is closest to it.

By comparing the resulting planes between the two datasets, it becomes possible to quantify the angular deviations or tilting that occurred over time at the individual cuboid level. These deviations were then analyzed in-depth to evaluate the structural changes or shifting within the breakwater.

3. Results and Discussion

3.1. Photogrammetric Reconstruction

The workflow outlined in Section 2.3 was applied to the two datasets obtained in their respective flight campaigns. All processing steps, as described in the preceding sections, were executed in ETRS89 (European Terrestrial Reference System 1989) with rectangular coordinates PTTM06 (Portugal Transverse Mercator 2006), EPSG: 3763. The orthometric height is referenced to the geoid model for mainland Portugal, GeodPT08 [55].

Both image orientation and the subsequent densification of the PC were performed within the automated pipeline of Metashape, selecting the "high" quality setting controls. With this option, the software operates with the original size of the photos, allowing for more detailed and accurate geometry, albeit at the cost of longer processing times. Table 4 summarizes the key characteristics of the photogrammetric processing for both time periods.

Although the flight planning files used in both flights were not exactly identical, the number of images and flight altitude remained reasonably consistent. This consistency is crucial when comparing data across multiple time periods, and whenever possible, equivalent parameters should be maintained, ideally by using the same waypoint file. This approach ensures that image resolutions, and consequently the resolutions of derived PCs, remain relatively uniform. Furthermore, employing the same technique for generating PCs and equivalent GCPs for georeferencing contributes to positional consistency in the resulting photogrammetric products. When PC sources are different, preprocessing steps are often required before applying any change detection algorithm [56]. In contrast, in this case, intermediate co-registration processes can be skipped, making PC data from different time periods directly comparable.

Table 4. Summary of photogrammetric processing results.

			Flight #1	Flight #2
		# of images	249	237
		Mean flight height (m)	30.9	29.6
		GSD (mm)	8.7	8.0
		Key points	206,882	212,619
		Dense cloud size (points)	23,119,079	23,645,284
	Residuals from GCPs (mm)	X	3.8	6.5
		Y	6.1	17.8
		Z	7.6	9.7
	Accuracy from CPs (mm)	X	7.2	6.8
		Y	8.9	11.4
		Z	6.6	14.3
		DEM resolution (mm/pix)	34.9	32.5

PC#1

PC#2

As a reference for further comparison with the proposed RANSAC-based method, we also generated the DoD map (Figure 4) by deriving the differences between the two DEMs, each with resolutions better than 3.5 cm/pix, as shown in Table 4. The DoD provides a straightforward representation of surface elevation changes, making it rather easy to detect and visualize areas experiencing severe alterations. However, even in these cases, obtaining a precise interpretation of the number of shifted blocks is challenging using this approach.
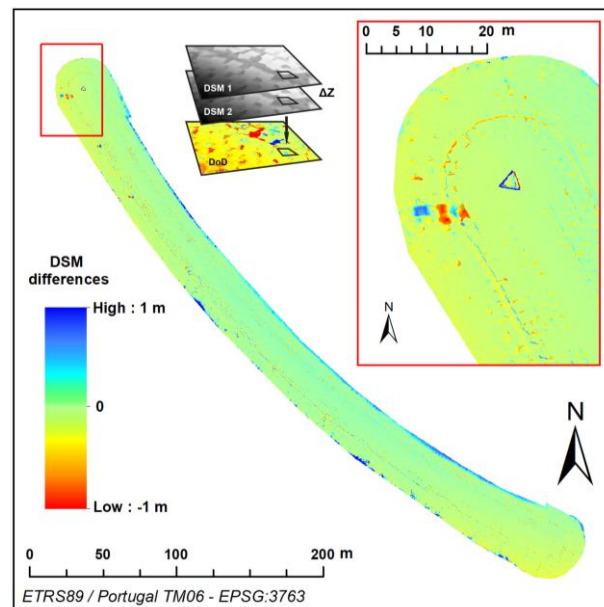
Figure 4. Global DoD. The detail view illustrates the NW head of the RMB showing some accreted and eroded areas that hint at the displacement of some CAUs.

3.2. RANSAC-Based Analysis

3.2.1. PC Segmentation

The PC segmentation process was implemented following the methodology described above to fit planes to the PC data (Figure 5). While applying the RANSAC algorithm, the largest planes in the original PC (Figure 5a), corresponding to the top concrete platform of the RMB, were also detected, as illustrated by the pink, orange, and green patches in Figure 5b. These planes were subsequently removed from the classified data, retaining only the planes representing the CAUs.

Additional challenges associated with the use of RANSAC are depicted in Figure 5c,d. In some instances, planes were fitted across the surfaces of multiple cuboids due to their proximity or similar elevations. This phenomenon is predominantly observed in the upper zone of the RMB, where the CAUs were initially placed level, and due to the stability of these areas, they remain mostly level. Moreover, the narrow gaps between neighboring armor units often go unsampled, consolidating several wave-dissipating block poses into a singular representation, as highlighted by previous studies utilizing alternative methodologies [57,58]. Conversely, there are cases wherein finding a suitable plane representing specific cuboids proves challenging. This occurs predominantly at the lower levels of the RMB, where the PC exhibits lower quality and increased noise due to degraded texture of the cuboids in these areas and the presence of water, algae, etc.
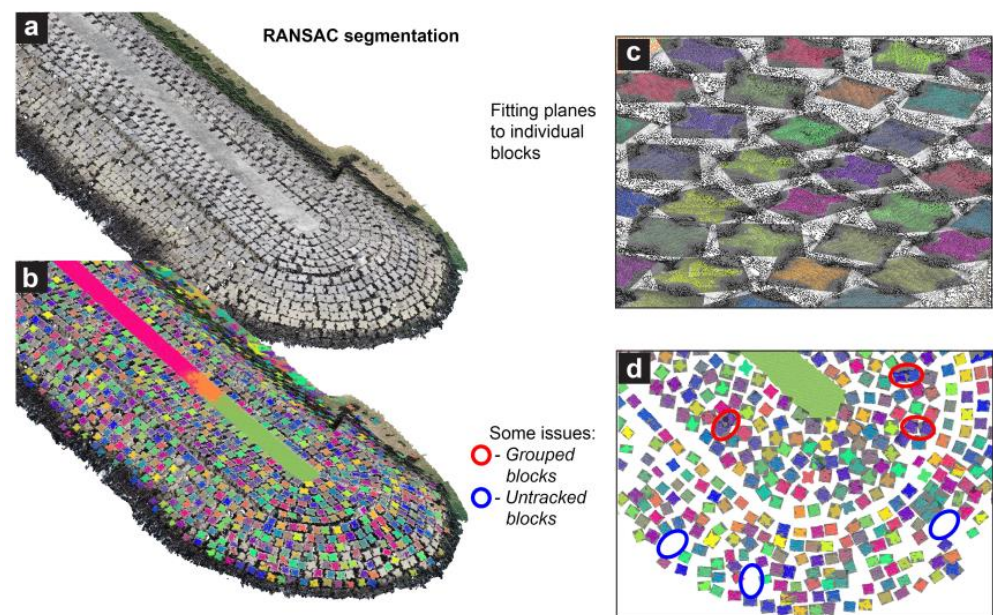
Figure 5. RANSAC segmentation: (**a**) RAW point cloud; (**b**,**c**) point cloud segmented into planes, and (**d**) examples of how some parameter settings produce issues affecting the precision of the segmentation. The colors of planes are assigned arbitrarily for differentiation purposes.

The process of determining appropriate fitting parameters has been carried out iteratively, involving trials with gradual refinement until reasonably satisfactory results were achieved in terms of meaningful interpretation and comprehensiveness. The best outcomes, based on these criteria, were obtained with a minimum support points per plane of 200 and a maximum distance to the fitting plane of 0.005 m. The maximum allowable deviation in the normal direction of the plane from the estimated normal was set to 5°. The overlooking probability value was set to 0.0001, aiming to work with a low probability of missing outliers during the RANSAC plane fitting process.

To evaluate the accuracy of the RANSAC results, we chose a representative sampling area in the southeast quadrant of the RMB, encompassing approximately 1037 CAUs, which accounts for roughly a quarter of the total number of armor units. To prevent the inclusion of flooded areas, cuboids situated at elevations lower than 0 m AMSL were excluded from the sampling. As illustrated in Figure 6, a manual sampling of this zone was performed to verify the correct classification of planes in both time periods.

Items classified as True Positives (TP) correspond to actual cuboids correctly modeled by a plane. False Positives (FP) refer to detected planes that do not precisely correspond to the top face of an individual wave-dissipating block. A significant portion of items falling into this category consists of planes fitted to the lateral faces of some cuboids. False Negatives represent actual CAUs that were not detected as planes by the RANSAC fitting, so they were manually added to account for their number. A single plane fitting two (or more) cuboids has been considered in terms of counting as two (or more) FNs. Lastly, the concept of True Negative (TN) is somewhat more abstract and includes non-cuboids correctly classified as such. As shown in Figure 6, this class includes manually added elements like large rocks within inter-block spaces, which the algorithm correctly identified as non-cuboids.

Table 5 shows the confusion matrix containing TP, TN, FP, and FN values. These values are components of the confusion matrix which defines actual and predicted classes.
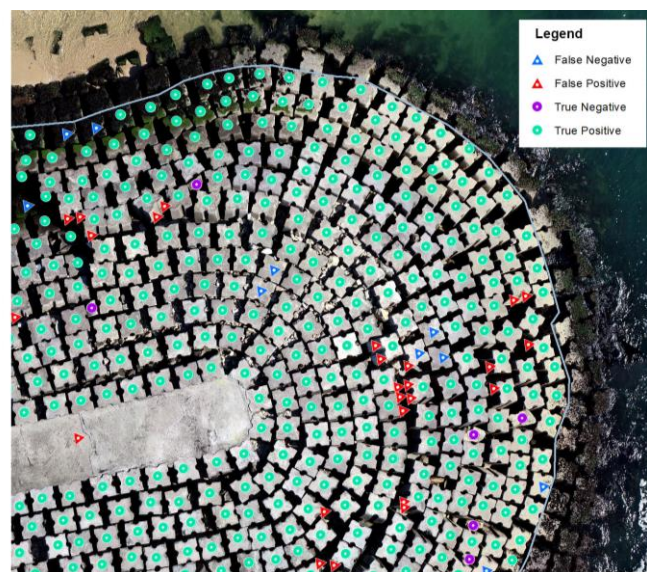
Figure 6. Post-classification accuracy assessment.

Table 5. Confusion matrix.

		Predicted Class					
	True positives		False negatives		Positive		
	PC#1	932	PC#1	41	PC#1	973	
	PC#2	882	PC#2	68	PC#2	950	
		1814		109		1923	
	False positives		True negatives		Negative		
	PC#1	51	PC#1	12	PC#1	63	
	PC#2	66	PC#2	21	PC#2	87	
		117		33		150	
	Positive		Negative				
	PC#1	983	PC#1	53			
	PC#2	948	PC#2	89			
		1931		142			

(Actual class)

Sensitivity, specificity, precision, negative predictive value, and accuracy can be easily derived from the confusion matrix values, with the formulas mentioned in Table 6:

Table 6. Performance indicators based on the TP, FP, TN, and FN parameters [59].

$Sensitivity = \frac{TP}{TP+FN}$	(3)
$Specificity = \frac{TN}{TN+FP}$	(4)
$Precision = \frac{TP}{TP+FP}$	(5)
$Accuracy = \frac{TP+TN}{N}$	(6)

Sensitivity, representing the percentage of positive cases, is 94%, while specificity, the percentage of negative cases, is 22% in our experiment. Precision achieved 94%, and accuracy, indicating the percentage of correctly identified cases, is 89%.

While these results are promising, there is potential for improvement in the method, especially in reducing FPs associated with detecting lateral faces on the CAUs. Moreover, the count of FNs is relatively high, mainly due to planes fitted to multiple Antifer blocks simultaneously. Conducting lower altitude flights with higher PC resolution could potentially enhance the detection of discontinuities between cuboids and improve sensitivity to detect outliers based on the distance to the planes.

3.2.2. RMB Stability Assessment

The maximum consensus planes obtained by applying the RANSAC algorithm to each of the dense PCs were cross-referenced through a proximity-based criterion. Through this spatial join or alignment process, a total of 3697 pairs of corresponding planes were identified across the entire surface of the breakwater.

While the correlation method used here is advantageous due to its inherent simplicity, it is not without its drawbacks. The effectiveness of this method relies significantly on the precision of the RANSAC algorithm in detecting and segmenting planes. Any inaccuracies in the segmentation of either PC, such as FPs or FNs, directly impact the subsequent plane matching phase. Essentially, an orphan plane, which exists in one dataset without a counterpart in the other, may be matched with the nearest available plane. This could result in semantic inconsistencies and distort subsequent analyses, although it does provide the advantage of generating a comprehensive and continuous dataset. To address these issues, the spatial join tool introduces a distance field within the outcome, representing the spatial closeness of linked geometries. This enables the definition of a specific tolerance threshold to prevent these inconsistencies.

The normal vectors of the fitted planes for each corresponding pair of block faces can be acquired to estimate the tilt angle within a single block. Figure 7 illustrates the overall inclination values obtained for each cuboid in the RMB, categorized based on their magnitudes.
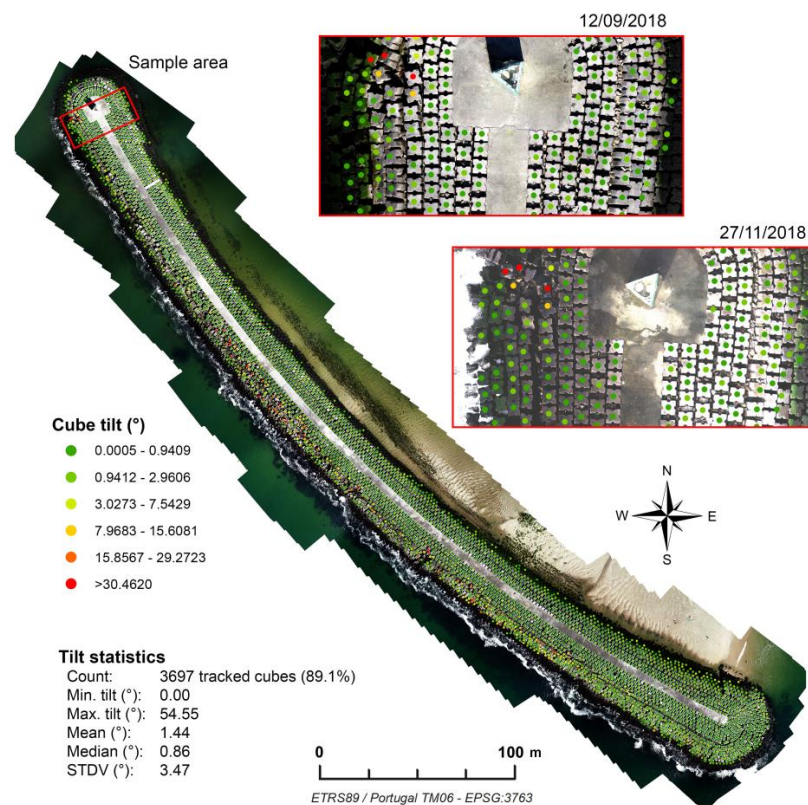

Figure 7. Overall inclination map based on the RANSAC-based method. The colors represent the magnitude of rotations.

In the graphics presented in Figure 8, a more detailed breakdown of these inclinations, considering both magnitude and inclination direction, is provided. Analysis of these figures allows us to deduce that the most significant instabilities of the blocks occur in the predominant southwest (SW) direction, aligning with the most exposed flank of the breakwater. Some tilting of the cuboids is also noticeable in the northeast (NE) body of the RMB, although the movements detected here are generally much smaller. In terms of

magnitude, it is observed that 61.1% of the wave-dissipating blocks undergo rotations of zero or less than 1°, and 91.7% experience movements of less than 2° based on data derived from the RANSAC method. However, it is worth noting that rotations of certain CAUs can, in specific cases, exceed 50°.
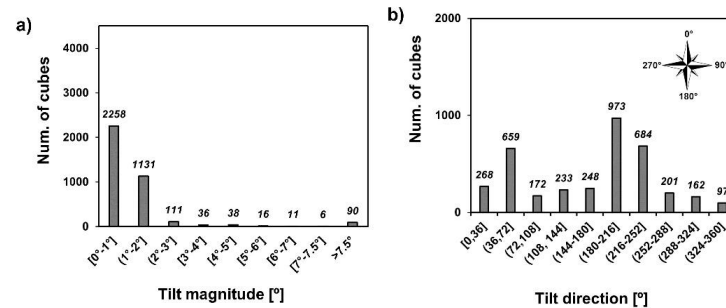

Figure 8. Overall tilt analysis of the identified cuboids: (**a**) magnitude and (**b**) direction of rotations.

In Figure 9, an illustrative region displaying relatively stable blocks within the southwest (SW) body is presented. Evaluating displacements or rotations solely through a visual examination of orthophotos from two different time periods poses a significant challenge. Factors like variations in imaging texture due to cuboid shading, the presence of biofilm, algae, etc., add complexity to the visual comparison of the orthophotos. Nonetheless, careful observation may suggest some rotation in the lower-right cuboid of the image.
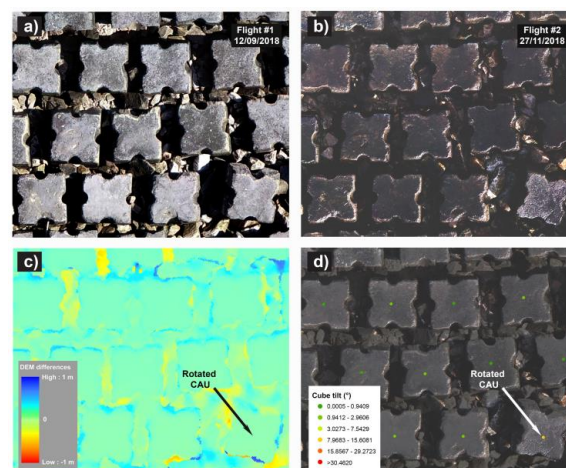

Figure 9. Comparison of DoD vs. RANSAC-based methods. Orthophotos corresponding to (**a**) the first flight (pre-storm) and (**b**) the second flight (post-storm), (**c**) DSM subtraction (DoD), and (**d**) tilting results measured with the RANSAC-based approach.

In the case of DoD, discerning any form of displacement or rotation is challenging, especially for cuboids with significant displacements. Unlike cuboids with noticeable movements, it is difficult to infer any changes in the elevations of rotated CAUs, as these elevations may remain relatively stable despite the rotation. Some elevation fluctuations are observable within inter-block spaces, potentially attributed to the movement of small stones in the underlayer or artifacts in the DSMs caused by occluded regions. The DoD represents elevation changes on a cell-by-cell basis, typically along a predefined direction, often the Z-axis (vertical direction). While the simplicity of the DoD method is advantageous, it does have limitations in intricate contexts, such as overhangs and nearly vertical slopes, where vertical differences may not provide comprehensive insights. Similar findings have been reported in previous studies [60]. Consequently, the precision of interpreting elevation differences along the edges of each CAU is not entirely accurate when using a traditional

2.5D method for change detection like DoD. As illustrated in Figure 9d, the RANSAC-based plane-fitting method demonstrates increased sensitivity, showcasing its effectiveness even in more stable regions of the RMB model.

Operating at the level of individual cuboids, the proposed methodology allows for a more detailed analysis of the structure. The graphs in Figure 10 present both a global analysis (Figure 10a) and a zonal breakdown of cuboid counts against their detected inclinations. The zonal analysis divides the total count of CAUs into five principal zones characterizing the RMB. The crest of the detached breakwater, referred to as RMB top, spans its entire length and includes three rows of wave-dissipating blocks on each side of the central platform. Due to the substantial number of blocks within this area, it exhibits a relatively low occurrence of CAU inclinations, as illustrated in Figure 10b. In the breakwater heads (Figure 10c,d), a limited number of units exhibit relatively high shifts, primarily found in the northwest (NW) head. Furthermore, the southwest (SW) body zone shows significantly higher CAU inclinations than the inner breakwater region (Figure 10e,f), which is consistent with its exposure to wave action. Beyond this simplified examination, the results underscore the potential of these methods to provide quantitative assessments of the extent of damage.
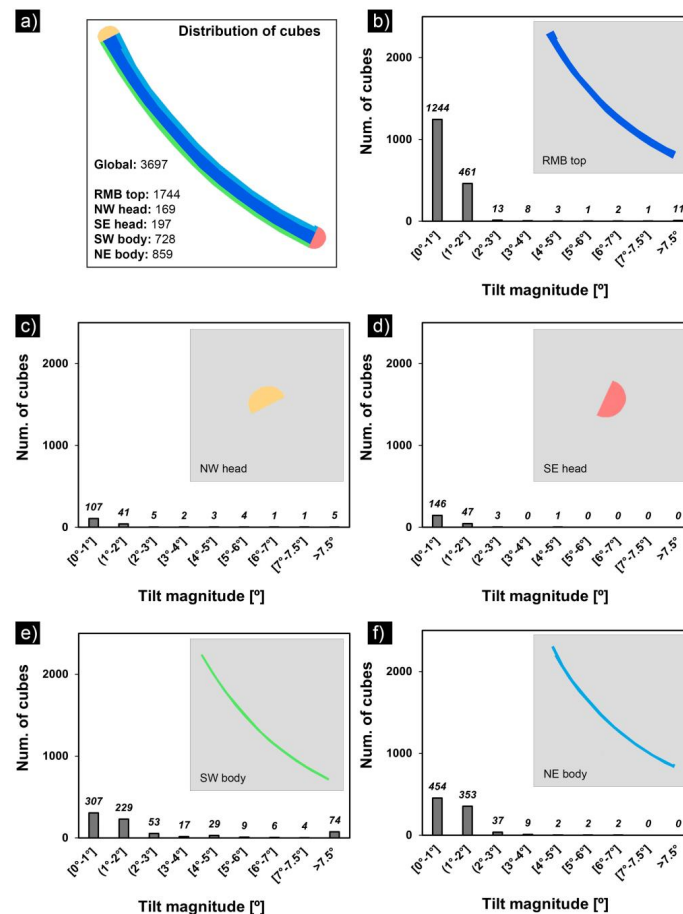

Figure 10. Zonal stability analysis of breakwater. (**a**) Overall distribution of tracked Antifer cubes and zonal tilt measurements in (**b**) RMB top, (**c**) NW head, (**d**) SE head, (**e**) SW body, and (**f**) NE body.

4. Conclusions and Future Remarks

The evaluation of structural changes and tilting in coastal structures, particularly breakwaters, is crucial for ensuring their long-term stability. The integration of aerial imagery, photogrammetric reconstruction, and RANSAC-based segmentation provides an intriguing tool for the continuous monitoring and assessment of breakwater stability.

While DoD remains a prevalent method for analyzing multi-temporal changes due to its simplicity, it has limitations. DEMs inherently lack complete 3D spatial information and may struggle to differentiate individual armor units, leading to reduced accuracy in change detection. This limitation becomes particularly evident in scenarios involving vertical shifts, rotations, or tilting of individual cuboids. The results of this study demonstrate that the proposed approach based on RANSAC is more effective than DEM-based methods in detecting even subtle tilting. This approach provides a detailed and localized understanding of the structural integrity of the breakwater. By enhancing the ability to detect and comprehend structural changes in the RMB over time, it contributes to improved coastal infrastructure management and resilience.

Further improvement and validation of the methodology should focus on obtaining unambiguous matches between CAUs in different epochs. It would also be desirable to refine segmentation accuracy, possibly by integrating the RANSAC method with image-based approaches, such as using detectors and feature extractors for block edges. Additionally, exploring the adaptability of this approach to more intricate shapes of the armor units by fitting other geometric primitives presents an interesting avenue for research.

References

1. Akarsh, P.K.; Chaudhary, B. Review of Literature on Design of Rubble Mound Breakwaters. In Proceedings of the International Conference on Civil Engineering Trends and Challenges for Sustainability, Bapatla, India, 24–25 September 2021; pp. 775–796.
2. Nguyen, D.V.; Van Gelder, P.H.A.J.M.; Verhagen, H.J.; Vrijling, J.K. Optimal inspection strategy for rubble-mound breakwaters with time-dependent reliability analysis. In *Relaibility, Risk and Safety*; Taylor & Francis Group: London, UK, 2010; pp. 1409–1415.
3. Etemad-Shahidi, A.; Bali, M.; van Gent, M.R.A. On the stability of rock armored rubble mound structures. *Coast. Eng.* **2020**, *158*, 103655. [CrossRef]
4. der Meer, J.W. Conceptual design of rubble mound breakwaters. In *Advances in Coastal And Ocean Engineering*; World Scientific: London, UK, 1995; Volume 1, pp. 221–315.
5. Puente, I.; Lindenbergh, R.; González-Jorge, H.; Arias, P. Terrestrial laser scanning for geometry extraction and change monitoring of rubble mound breakwaters. *ISPRS Ann. Photogramm. Remote Sens. Spat. Inf. Sci.* **2014**, *2*, 289–295. [CrossRef]
6. Campos, Á.; Molina-Sanchez, R.; Castillo, C. Damage in rubble mound breakwaters. Part II: Review of the definition, parameterization, and measurement of damage. *J. Mar. Sci. Eng.* **2020**, *8*, 306. [CrossRef]
7. Musumeci, R.E.; Moltisanti, D.; Foti, E.; Battiato, S.; Farinella, G.M. 3-D monitoring of rubble mound breakwater damages. *Meas. J. Int. Meas. Confed.* **2018**, *117*, 347–364. [CrossRef]
8. Lemos, R.; Peña, E.; Santos, J.; Sande, J.; Figuero, A.; Alvarellos, A.; Laiño, E.; Reis, M.T.; Fortes, C.J.; Kerpen, N.B.; et al. 3D Survey Modelling for Damage Assessment in Rubble-Mound Breakwaters Under Oblique Wave Incidence. *Ital. J. Eng. Geol. Environ.* **2020**, *20*, 73–85. [CrossRef]
9. Lemos, R.; Fortes, C.; Silva, G.; Pinheiro, L. An estimation of the damage of scale models of breakwaters using the time of flight method. *Rev. Mecânica Exp.* **2022**, *35*, 49–58.
10. Lemos, R.; Santos, J.A.; Fortes, C.J.E.M. Damage Evolution Prediction during 2D Scale-Model Tests of a Rubble-Mound Breakwater: A Case Study of Ericeira's Breakwater. *Modelling* **2022**, *4*, 1–18. [CrossRef]
11. Vieira, F.; Taveira-Pinto, F.; Rosa-Santos, P. Damage evolution in single-layer cube armoured breakwaters with a regular placement pattern. *Coast. Eng.* **2021**, *169*, 103943. [CrossRef]
12. Lemos, R.; Loja, M.A.R.; Rodrigues, J.; Rodrigues, J.A. Photogrammetric analysis of rubble mound breakwaters scale model tests. *AIMS Environ. Sci.* **2016**, *3*, 541–559. [CrossRef]
13. Fortes, C.J.E.M.; Lemos, R.; Mendonça, A.; Reis, M.T. Damage progression in rubble-mound breakwaters scale model tests, under a climate change storm sequence. *Res. Eng. Struct. Mater.* **2019**, *5*, 415–426. [CrossRef]

14. Marino, S.; Galantucci, R.A.; Saponieri, A. Measuring rock slope damage on rubble mound breakwater through digital photogrammetry. *Meas. J. Int. Meas. Confed.* **2023**, *211*, 112656. [CrossRef]
15. Mishra, V.; Avtar, R.; Prathiba, A.P.; Mishra, P.K.; Tiwari, A.; Sharma, S.K.; Singh, C.H.; Chandra Yadav, B.; Jain, K. Uncrewed Aerial Systems in Water Resource Management and Monitoring: A Review of Sensors, Applications, Software, and Issues. *Adv. Civ. Eng.* **2023**, *2023*, 3544724. [CrossRef]
16. Robin, N.; Levoy, F.; Anthony, E.J.; Monfort, O. Sand spit dynamics in a large tidal-range environment: Insight from multiple LiDAR, UAV and hydrodynamic measurements on multiple spit hook development, breaching, reconstruction, and shoreline changes. *Earth Surf. Process. Landforms* **2020**, *45*, 2706–2726. [CrossRef]
17. Gonçalves, J.A.; Henriques, R. UAV photogrammetry for topographic monitoring of coastal areas. *ISPRS J. Photogramm. Remote Sens.* **2015**, *104*, 101–111. [CrossRef]
18. Stagnitti, M.; Musumeci, R.E.; Foti, E. Surface roughness measurement for the assessment of damage dynamics of existing and upgraded cube-armored breakwaters. *Coast. Eng.* **2023**, *179*, 104226. [CrossRef]
19. King, S.; Leon, J.; Mulcahy, M.; Jackson, L.A.; Corbett, B. Condition survey of coastal structures using UAV and photogrammetry. In Proceedings of the Australasian Coasts & Ports Conference, Twin Waters, Australia, 15–18 August 2017; pp. 704–710.
20. Rezaldi, M.Y.; Yoganingrum, A.; Hanifa, N.R.; Kaneda, Y.; Kushadiani, S.K.; Prasetyadi, A.; Nugroho, B.; Riyanto, A.M. Unmanned aerial vehicle (Uav) and photogrammetric technic for 3d tsunamis safety modeling in cilacap, indonesia. *Appl. Sci.* **2021**, *11*, 11310. [CrossRef]
21. Layek, S.; Villuri, V.G.K.; Koner, R.; Chand, K. Rainfall & Seismological Dump Slope Stability Analysis on Active Mine Waste Dump Slope with UAV. *Adv. Civ. Eng.* **2022**, *2022*, 5858400. [CrossRef]
22. Kim, K.; Francis, O. Integration of In-Situ, Laboratory and Computer Models for Coastal Risk Assessment, Planning and Development. In Proceedings of the Ocean 2018 MTS/IEEE Charleston, Charleston, SC, USA, 22–25 October 2018; pp. 1–5. [CrossRef]
23. Henriques, M.J.; Lemos, R.; Capitão, R.; Fortes, C.J. The monitoring of rubble mound breakwaters. An assessment of UAV technology. In Proceedings of the 7th International Conference on Engineering Surveying, Lisbon, Portugal, 18–20 October 2017; pp. 1–8.
24. Gonçalves, D.; Gonçalves, G.; Pérez-Alvávez, J.A.; Andriolo, U. On the 3D Reconstruction of Coastal Structures by Unmanned Aerial Systems with Onboard Global Navigation Satellite System and Real-Time Kinematics and Terrestrial Laser Scanning. *Remote Sens.* **2022**, *14*, 1485. [CrossRef]
25. Gonçalves, D.; Gonçalves, G.; Pérez-Alvárez, J.; Cunha, M.C.; Andriolo, U. Combining Unmanned Aerial Systems and Structure from Motion Photogrammetry To Reconstruct the Geometry of Groins. *Int. Arch. Photogramm. Remote Sens. Spat. Inf. Sci. ISPRS Arch.* **2022**, *43*, 1003–1008. [CrossRef]
26. Hussain, M.; Chen, D.; Cheng, A.; Wei, H.; Stanley, D. Change detection from remotely sensed images: From pixel-based to object-based approaches. *ISPRS J. Photogramm. Remote Sens.* **2013**, *80*, 91–106. [CrossRef]
27. Blaschke, T.; Hay, G.J.; Kelly, M.; Lang, S.; Hofmann, P.; Addink, E.; Queiroz Feitosa, R.; van der Meer, F.; van der Werff, H.; van Coillie, F.; et al. Geographic Object-Based Image Analysis—Towards a new paradigm. *ISPRS J. Photogramm. Remote Sens.*p **2014**, *87*, 180–191. [CrossRef]
28. Kundal, S.; Chowdhury, A.; Bhardwaj, A.; Garg, P.K.; Mishra, V. GeoBIA-based semi-automated landslide detection using UAS data: A case study of Uttarakhand Himalayas. *SPIE Future Sens. Technol.* **2023**, *12327*, 79.
29. Sharma, S.K.; Jain, K.; Shukla, A.K. A Comparative Analysis of Feature Detectors and Descriptors for Image Stitching. *Appl. Sci.* **2023**, *13*, 6015. [CrossRef]
30. Chen, L.; Rottensteiner, F.; Heipke, C. Feature detection and description for image matching: From hand-crafted design to deep learning. *Geo-Spatial Inf. Sci.* **2021**, *24*, 58–74. [CrossRef]
31. Forero, M.G.; Mambuscay, C.L.; Monroy, M.F.; Miranda, S.L.; Méndez, D.; Valencia, M.O.; Selvaraj, M.G. Comparative analysis of detectors and feature descriptors for multispectral image matching in rice crops. *Plants* **2021**, *10*, 1–24. [CrossRef] [PubMed]
32. Qin, R.; Tian, J.; Reinartz, P. 3D change detection—Approaches and applications. *ISPRS J. Photogramm. Remote Sens.* **2016**, *122*, 41–56. [CrossRef]
33. Williams, R.D. DEMs of difference. *Geomorphol. Tech.* **2012**, *2*, 1–17.
34. Lemos, R.; Capitão, R.; Fortes, C.; Henriques, M.; Silva, L.G.; Martins, T. A methodology for the evaluation of evolution and risk of breakwaters. Application to Portimão harbor and of Faro-Olhão inlet. *J. Integr. Coast. Zone Manag.* **2020**, *20*, 103–119. [CrossRef]
35. Bueno Esposito, M.; Díaz-Vilariño, L.; Martínez-Sánchez, J.; González -Jorge, H.; Arias, P. 3D reconstruction of cubic armoured rubble mound breakwaters from incomplete lidar data. *Int. J. Remote Sens.* **2015**, *36*, 5485–5503. [CrossRef]
36. Xu, Y.; Kanai, S.; Date, H.; Sano, T. Deep-Learning-Based Three-Dimensional Detection of Individual Wave-Dissipating Blocks from As-Built Point Clouds Measured by UAV Photogrammetry and Multibeam Echo-Sounder. *Remote Sens.* **2022**, *14*, 5575. [CrossRef]
37. Shen, Y.; Lindenbergh, R.; Wang, J.; Ferreira, V.G. Extracting individual bricks from a laser scan point cloud of an unorganized pile of bricks. *Remote Sens.* **2018**, *10*, 11709. [CrossRef]
38. Shen, Y.; Wang, J.; Puente, I. A Novel Baseline-Based Method to Detect Local Structural Changes in Masonry Walls Using Dense Terrestrial Laser Scanning Point Clouds. *IEEE Sens. J.* **2020**, *20*, 6504–6515. [CrossRef]
39. Choi, S.; Kim, T.; Yu, W. Performance evaluation of RANSAC family. *J. Comput. Vision* **1997**, *24*, 271–300. [CrossRef]

40. Huber, P.J.; Ronchetti, E.M. *Robust Statistics*; Wiley: Hoboken, NJ, USA, 1981; Volume 1.
41. Rousseeuw, P.J. Least median of squares regression. *J. Am. Stat. Assoc.* **1984**, *79*, 871–880. [CrossRef]
42. Borrmann, D.; Elseberg, J.; Lingemann, K.; Nüchter, A. The 3d hough transform for plane detection in point clouds: A review and a new accumulator design. *3D Res.* **2011**, *2*, 1–13. [CrossRef]
43. Mahendran, S.; Ali, H.; Vidal, R. 3D Pose Regression Using Convolutional Neural Networks. In Proceedings of the IEEE International Conference on Computer Vision Workshops, Honolulu, HI, USA, 21–26 July 2017; pp. 494–495. [CrossRef]
44. Fischler, M.A.; Bolles, R.C. Random sample consensus: A Paradigm for Model Fitting with Applications to Image Analysis and Automated Cartography. *Commun. ACM* **1981**, *24*, 381–395. [CrossRef]
45. Schnabel, R.; Wahl, R.; Klein, R. Efficient RANSAC for point-cloud shape detection. *Comput. Graph. Forum* **2007**, *26*, 214–226. [CrossRef]
46. Gonultas, F.; Atik, M.E.; Duran, Z. Extraction of Roof Planes from Different Point Clouds Using RANSAC Algorithm. *Int. J. Environ. Geoinformatics* **2020**, *7*, 165–171. [CrossRef]
47. Li, Z.; Shan, J. RANSAC-based multi primitive building reconstruction from 3D point clouds. *ISPRS J. Photogramm. Remote Sens.* **2022**, *185*, 247–260. [CrossRef]
48. Wang, S.; Zhang, Z.; Wang, C.; Zhu, C.; Ren, Y. Multistep rocky slope stability analysis based on unmanned aerial vehicle photogrammetry. *Environ. Earth Sci.* **2019**, *78*, 260. [CrossRef]
49. Giulietti, N.; Allevi, G.; Castellini, P.; Garinei, A.; Martarelli, M. Rivers' Water Level Assessment Using UAV Photogrammetry and RANSAC Method and the Analysis of Sensitivity to Uncertainty Sources. *Sensors* **2022**, *22*, 5319. [CrossRef] [PubMed]
50. Iglesias, I.; Venâncio, S.; Pinho, J.L.; Avilez-Valente, P.; Vieira, J.M.P. Two models solutions for the Douro estuary: Flood risk assessment and breakwater effects. *Estuaries Coasts* **2019**, *42*, 348–364. [CrossRef]
51. Jiménez-Jiménez, S.I.; Ojeda-Bustamante, W.; Marcial-Pablo, M.D.J.; Enciso, J. Digital terrain models generated with low-cost UAV photogrammetry: Methodology and accuracy. *ISPRS Int. J. Geo-Information* **2021**, *10*, 285. [CrossRef]
52. Calì, M.; Ambu, R. Advanced 3D photogrammetric surface reconstruction of extensive objects by UAV camera image acquisition. *Sensors* **2018**, *18*, 2815. [CrossRef] [PubMed]
53. Ortiz-Sanz, J.; Gil-Docampo, M.; Rego-Sanmartín, T.; Arza-García, M.; Tucci, G. A PBeL for training non-experts in mobile-based photogrammetry and accurate 3-D recording of small-size/non-complex objects. *Meas. J. Int. Meas. Confed.* **2021**, *178*, 109338. [CrossRef]
54. Carrilho, A.C.; Galo, M. Extraction of building roof planes with stratified random sample consensus. *Photogramm. Rec.* **2018**, *33*, 363–380. [CrossRef]
55. Catalão, J.; Sevilla, M.J. Mapping the geoid for Iberia and the Macaronesian Islands using multi-sensor gravity data and the GRACE geopotential model. *J. Geodyn.* **2009**, *48*, 6–15. [CrossRef]
56. Arza-García, M.; Gil-Docampo, M.; Ortiz-Sanz, J. A hybrid photogrammetry approach for archaeological sites: Block alignment issues in a case study (the Roman camp of A Cidadela). *J. Cult. Herit.* **2019**, *38*, 195–203. [CrossRef]
57. Soares, F.; Henriques, M.J.; Rocha, C. Concrete Block Tracking in Breakwater Models Concrete Block Tracking in Breakwater Models. In Proceedings of the FIG Working Week 2017, Helsinki, Finland, 29 May—2 June 2017; pp. 1–14.
58. Henriques, M.J.; Brás, N.; Roque, D.; Lemos, R.; Fortes, C.J.E.M. Controlling the Damages of Physical Models of Rubble-Mound Breakwaters by Photogrammetric Products-Orthomosaics and Point Clouds. In Proceedings of the Proceedings of the 3rd Joint International Symposium on Deformation Monitoring, Viena, Austria, 30 March–1 April 2016; p. 8.
59. Powers, D.M.W. Evaluation: From Precision, Recall and F-Factor to ROC, Informedness, Markedness & Correlation. Technical Report SIE-07-001. *arXiv* **2007**, arXiv:2010.16061v1.
60. Kharroubi, A.; Poux, F.; Ballouch, Z.; Hajji, R.; Billen, R. Three Dimensional Change Detection Using Point Clouds: A Review. *Geomatics* **2022**, *2*, 457–485. [CrossRef]